Research Square

Preprints are preliminary reports that have not undergone peer review.
They should not be considered conclusive, used to inform clinical practice,
or referenced by the media as validated information.

Particle size evolution during the preparation of NTC thermosensitive ceramics from nanopowders and its influence on the structure and properties

Yan ZHAO

yanzhao@ms.xjb.ac.cn

Xinjiang Technical Institute of Physics & Chemistry of CAS

Zhenzhen HUO

Xinjiang Technical Institute of Physics & Chemistry of CAS

Qing ZHAO

Xinjiang Technical Institute of Physics & Chemistry of CAS

Yuling TUO

Xinjiang Technical Institute of Physics & Chemistry of CAS

Zhaowen SHAO

Xinjiang Technical Institute of Physics & Chemistry of CAS

Aimin CHANG

Xinjiang Technical Institute of Physics & Chemistry of CAS

Research Article

Keywords: thermosensitive ceramics, high-energy ball milling, lattice defects, phase evolution, densification, electrical properties

Posted Date: May 27th, 2026

DOI: https://doi.org/10.21203/rs.3.rs-9660492/v1

License: This work is licensed under a Creative Commons Attribution 4.0 International License.
Read Full License

Additional Declarations: No competing interests reported.

Version of Record: A version of this preprint was published at Journal of Materials Science: Materials in Electronics on November 2nd, 2026. See the published version at https://doi.org/10.1007/s10854-026-18791-8.

Particle size evolution during the preparation of NTC thermosensitive ceramics from nanopowders and its influence on the structure and properties

Yan ZHAO [a]*, Zhenzhen HUO [a b], Qing ZHAO [a], Yuling TUO[a], Zhaowen SHAO [a], Aimin CHANG [a]*

[a] Key Laboratory of Functional Materials and Devices for Special Environments of CAS, Xinjiang Key Laboratory of Electronic Information Materials and Devices, Xinjiang Technical Institute of Physics & Chemistry of CAS, Urumqi, 830011, China

[b] Center of Materials Science and Optoelectronics Engineering, University of Chinese Academy of Sciences, Beijing, 100049, China

* Corresponding author. Email: yanzhao@ms.xjb.ac.cn; changam@ms.xjb.ac.cn.

Abstract

In this study, the evolution of particle size during processing of nano-sized oxides was systematically investigated during the processing of Mn-Co-Ni-O-based spinel ceramics. And two different approaches - high-energy milling (HM) versus conventional milling (PM) - were compared in terms of their effects on the microstructure and electrical properties. Particle size after pre-sintering and re-milling was tracked by laser diffraction. Phase structure and microstructure were characterized by XRD, SEM, and TEM. The thermistor constant and activation energy were obtained via Arrhenius fitting. The resulting Nyquist plots were analyzed by equivalent circuit fitting to link microstructure with electrical properties. The initial nano-sized oxide (about 50 nm) was found to coarsen severely to 955.4 nm after pre-calcination. HM

successfully refined the particle size back to the nanoscale (D_{50}: 58-78 nm), while introducing a high density of intragranular dislocations, rough particle surfaces. The increased internal energy drives the powder into a non-equilibrium, metastable state, which gives a strong, continuous exothermic signal between ~ 800 K- 1500 K during thermal analysis. At 1250 °C, phase separation was detected by XRD in the HM samples, which transforms back to the equilibrium spinel phase at 1280 °C. The small-polaron hopping mechanism, measured on thermistors sintered at 1250 °C, does not depend on the milling process. Based on the analysis of Nyquist plots via equivalent circuit fitting, the phase separation turns out to be merely a kinetic by-product and does not affect grain boundary conduction. As a result, HM samples show a slightly lower grain boundary resistivity (R_{gb}) due to higher density. Consequently, the B value is not significantly affected. These findings establish a new paradigm for microstructure engineering of thermosensitive ceramics that goes beyond simple precursor particle size control, and provide solid experimental support for the precise tailoring of such microstructures.

Keywords: thermosensitive ceramics; high-energy ball milling; lattice defects; phase evolution; densification; electrical properties.

1. Introduction

Driven by the trend toward miniaturization and intellectualization in electronics, there is a growing demand for high-performance NTC thermistors that combine high accuracy and sensitivity with long-term stability and reliability [1,2]. Owing to their

stable performance, Mn-Co-Ni-O-based spinel ceramics are widely used NTC (negative temperature coefficient) thermistors for temperature sensing and circuit compensation [3-5]. Previous studies indicate that Mn-based spinels, as polar ionic crystals, commonly host polarons, leading to a temperature-dependent conduction mechanism: large polaron (band migration) at low temperatures and small polaron (hopping) at high temperatures [6,7]. Therefore, the polaron hopping model in Mn-Co-Ni-O thermosensitive ceramics implies that their key electrical performance is collectively governed by the intrinsic crystal structure (cation distribution and valence) and the extrinsic microstructure (grain size, grain boundary properties, and densification) [8,9]. Consequently, for a given material, their electrical performance is determined by phase composition, grain boundary structure, densification level and defect distribution, all of which are closely related to powder processing history.

Powder preparation constitutes the initial stage in the fabrication of electronic ceramics. Despite difficulties in scaling up production and achieving homogeneous mixing of multiple components with methods like chemical co-precipitation, sol-gel, and hydrothermal synthesis, the solid-state reaction of oxide raw materials remains the primary method for preparing NTC thermosensitive ceramics [10-13]. Therefore, in the preparation of thermosensitive ceramics via the solid-state reaction method, the principal strategies for controlling ceramic grain size involve optimizing ball milling processes to reduce the particle size [14]. Followed by, dense, fine-grained microstructures are attainable through regulating the sintering duration or utilizing specialized sintering techniques such as hot pressing [15,16]. Currently, constrained by

factors such as processing efficiency and cost, atmospheric pressure sintering remains the primary method for obtaining thermosensitive ceramics. In resistive devices, especially those with complex powder compositions, relying solely on sintering temperature and time is insufficient for achieving the precise grain size control required for highly consistent and stable thermosensitive ceramics. Therefore, powder characteristics must be considered a governing factor in the process. Research by Wang Bing et al. [17] on $Mn_{1.1}Co_{1.5}Fe_{0.4}O_4$ spinel ceramics fabricated from micron- and nano-sized powders revealed that the raw oxide particle size significantly influences the final ceramics' grain size and morphology, such that the nano-powders developed a "concave platelet morphology" upon sintering, which in turn modified the electrical performance parameters and aging stability. The research by Hosseini et al. [18] indicates that the thermosensitive ceramics fabricated directly from primary nano-oxides exhibit significantly smaller fluctuations in the B constant and finer grain size compared to those prepared using mixed raw oxides with micrometer/nanometer-scale particles. In the solid-state reaction process for preparing thermosensitive ceramics, the high-temperature heating process is crucial for the formation of the target phase and structural densification. However, the evolution of particle size and related state of the powder during the solid-state reaction stage has long been overlooked. From the data and results of existing studies, it can be observed that when micron and nano-powders are subjected to identical thermal treatments, the resulting ceramics exhibit grains of comparable size [19].

While post-calcination ball milling is a conventional prerequisite, the intrinsic powder

properties evolved during this process directly dictate the microstructural homogeneity and functional reliability of the final thermosensitive ceramics. Although planetary ball milling is widely employed for powder refinement due to its operational simplicity, its limitations become significantly pronounced when applied to the deep processing of particles down to the nanometer scale (<50 nm). If the powder particles resulting from the solid-state reaction are predominantly nanoparticles, the competition mechanism between energy input and particle surface energy renders the system prone to falling into a dynamic equilibrium between 'fragmentation' and 'agglomeration', thereby reaching the well-known grinding limit. High-energy ball milling is widely adopted for particle nanocrystallization; however, the concomitant mechanical activation introduces inevitable lattice defects, whose intricate effects on phase stability, sintering behavior, and electrical transport remain inadequately understood.

To address this gap, the present work used raw nano-sized oxide powders as starting materials and investigated the evolution of particle size before and after the solid-state reaction. Based on the Mn-Ni-Co-O concentration triangle phase diagram, $Mn_{1.25}Ni_{0.75}CoO_4$ was selected as the target composition [20-22]. The particle size evolution during thermal treatment was systematically monitored using advanced analysis techniques, and a comparative characterization of the morphological and structural features induced by high-energy ball milling was conducted. Furthermore, a comparative analysis was performed on the phase composition and microstructure of ceramics sintered from powders processed by conventional planetary ball milling and high-energy ball milling, with special emphasis on how particle size variations

influence the microstructure and electronic properties of the thermosensitive ceramics. Ultimately, this work aims to provide a scientific basis for the precise regulation of powder characteristics and the fabrication of high-performance thermosensitive ceramic devices with tailored electro-thermal responses.

2. Experimental

2.1 Raw Materials

Nanoscale oxide powders were employed as primary raw materials. The starting nano-sized oxides-MnO_2 (>99.9%, 50 nm), Co_3O_4 (>99.9%, 50 nm), and Ni_2O_3 (>99.9%, 20~30 nm)-were commercially obtained from Aladdin®.

2.2 Fabrication Process

$Mn_{1.25}Ni_{0.75}CoO_4$ ceramics were synthesized via a conventional solid-state reaction route, as outlined in Fig. 1. Raw powders were weighed according to the target stoichiometry and homogenized via conventional planetary ball milling in anhydrous ethanol at 300 rpm for 12 h, with the addition of 3 wt% MA-AA copolymer as a dispersant. After drying and sieving, the mixture was calcined in alumina crucibles at 850°C for 2 h to carry out the solid-state reaction, the conditions of which for this composition have been detailed in previous studies [20]. The calcined powder was divided into two batches for secondary pulverization: conventional planetary ball milling and high-energy ball milling. High-energy ball milling was performed using a wet-grinding attritor (Union Process Inc., USA) with zirconia jars and balls. Planetary ball milling was carried out with a laboratory-scale planetary mill (YXQM-4L,

Changsha Miqi Instrument & Equipment Co., Ltd., China) using polytetrafluoroethylene (PTFE) jars and zirconia balls. The choice of milling medium differed between the two processes based on practical considerations. In planetary ball milling, anhydrous ethanol was used as it offers effective heat dissipation, which is critical for temperature control during milling. In high-energy ball milling, however, the use of anhydrous ethanol led to severe foaming, which adsorbed fine particles and compromised mixing uniformity while increasing material loss. Since the high-energy milling system was equipped with a circulating water-cooling jacket that adequately addressed heat dissipation, deionized water was selected as the medium for this process. After secondary milling, the slurries were dried, and the resulting powders were loaded into a 10 mm diameter die, pre-pressed hydraulically, and further consolidated by cold isostatic pressing. The green pellets were finally sintered at 1250°C or 1280°C for 2 h to obtain the sensing ceramic pellets. Three parallel samples were prepared for each condition, with the final sintered thickness ranging from 1.6 to 1.7 mm.

Silver electrodes were applied on both surfaces of sintered ceramics and cured at elevated temperature for electrical measurements.

2.3 Characterization and Property Measurements

Particle size evolution at critical stages (after pre-sintering and post-ball-milling) was tracked by laser diffraction using a Zetasizer Nano ZS90. The phase structure of the ceramic samples was identified by X-ray diffraction (XRD) on a Bruker D8 Advanced diffractometer with CuK_{α} radiation (λ=0.154056 nm). Data were collected in the 2θ

range of 20° to 90° at a scanning rate of 6°/min. Microstructural characterization was performed at multiple scales.

The morphology of both pre-sintered and re-milled powders, as well as the microstructure of the ceramic tablets, were examined using a Zeiss SUPRA55VP field-emission scanning electron microscope (FE-SEM). To evaluate the microstructure of the temperature-sensitive ceramic, the tablets were cross-sectioned, embedded in epoxy resin, and subjected to metallographic polishing. Subsequently, thermal etching was performed in a box furnace at 1000 °C for 7 min.

Transmission electron microscopy (TEM) was performed on a JEOL JEM-F200 to examine the internal grain structure of powder particles following the solid-state reaction. For TEM observation, a small amount of powder was dispersed in deionized water, subjected to ultra-sonication for 15 minutes, and a droplet of the suspension was deposited onto a carbon-coated copper grid and dried at room temperature.

The temperature-dependent resistance (R-T) characteristics of the ceramic pellets sintered at 1250 °C were measured from 223 K to 423 K using a high-precision thermostatic bath in conjunction with an Agilent digital multimeter (Agilent Keithley 2400, USA). Based on the electrical conduction activation characteristics of NTC thermistors-wherein the logarithmic relationship between resistivity and temperature follows the Arrhenius equation-the measured resistance-temperature data were linearly fitted to extract the thermistor constant B and the activation energy E_a. The detailed calculation and fitting procedures can be found elsewhere [23]. Furthermore, AC complex impedance analysis was carried out in the frequency range of 20 Hz ~ 10 MHz

at 233 K, 253 K, and 273 K to probe the structure-property relationship between the microstructure and electrical behavior of the ceramic samples. Equivalent circuit models were subsequently constructed to fit the acquired impedance data. The underlying principles of the fitting process and the methodologies for parameter extraction are described in the references [24-26].

3. Results and Discussion

3.1 Particle Size and Morphology Evolution

The evolution of particle size of the thermosensitive ceramic powder was monitored throughout the preparation process prior to pressing. Fig. 2 depicts the particle morphologies and the corresponding particle size distribution curves (with fitted results) following the solid-state reaction and secondary ball-milling step. The measurement results obtained by the laser particle size analyzer are presented in Table 1. High-energy ball milling (hereinafter abbreviated as HM) and conventional planetary ball milling (hereinafter abbreviated as PM). The starting oxide raw material exhibits a primary particle size of 50 nm (as specified by the supplier). After the solid-state reaction, the resulting pre-sintered powder yielded a median particle size (D_{50}) of 955.4 nm, with a D_{90} value of approximately 1106.4 nm. The high surface energy of the nano-powders drives mass transport via surface and grain boundary diffusion, leading to Ostwald ripening [27]. Concurrently, the inter-diffusion of cations required to form the spinel structure further promotes grain boundary migration. These processes synergistically accelerate grain growth, resulting in a more than 20-fold increase in

particle size during pre-sintering. As shown in Fig.2a, the pre-sintered powder consists of particles formed via the sintering and agglomeration of fine primary particles, a result of the solid-state reactions between the initial oxides during pre-sintering.

Since high temperatures cause nanoparticle sintering and growth, secondary ball milling is usually conducted post pre-sintering to refine the particle size for controlling the final ceramic grain size. This study implemented two different ball milling techniques. As evidenced by Fig. 2b and 2d, the milled powders display distinct differences in morphology and size distribution. As anticipated, calcination of nanopowders leads to particle coalescence. Conventional planetary ball milling proved ineffective in further reducing the size of these coalesced particles; while capable of disrupting agglomerates, it fails to break down the strongly adherent individual nanoparticles. Particle size analysis confirmed the absence of significant size reduction after milling, highlighting the inherent limitation of mechanical comminution once materials undergo partial sintering or form strong interparticle bonds. Notably, the milling process neither reduced the particle size nor compromised the crystalline structure. TEM analysis (Fig. 2c) clearly reveals intact grains and a distinct diffraction pattern, confirming that the crystal integrity is fully preserved. Fig. 2d reveals that the powder particles after high-energy ball milling exhibit the characteristic morphology of mechanical fracturing, with irregular particle contours. The high-energy ball milled powder achieved a particle size of D_{50} at 58~78 nm and D_{90} at 78~91 nm, reaching the nanoscale again.

3.2 Lattice Defects Introduced by High-Energy Ball Milling

As presented in Fig. 2d, high-energy ball milling not only reduces the particle size to below 100 nm but also induces pronounced structural transformations within the particles. As shown in Fig. 2e, the milled powders exhibit significantly refined grains with a high density of internal dislocations. Correspondingly, the selected area electron diffraction (SAED) pattern displays discontinuous arcs - indicating a limited number of nanocrystallites with random orientations - and the arcs are noticeably broadened, reflecting extensive lattice imperfections [28]. This microstructural state contrasts sharply with conventionally milled powders, which preserve an intact lattice and yield regular SAED spots. Indeed, such structural evolution is rooted in the extreme mechanical energy imparted during collisions, which elevates the system's free energy and drives the powder into a non-equilibrium, metastable state. This stored internal energy - comprising dislocation networks, grain boundaries, and micro-strain - represents the intrinsic characteristics imparted by high-energy ball milling, distinguishing it from conventional milling.

3.3 Thermal behavior during sintering

Fig. 3 presents the DSC curves during high-temperature densification sintering of pre-sintered powders that were again subjected to HM and PM ball milling to reduce particle size. The PM sample shows a broad endothermic signal between 800 K and 1300 K, characteristic of conventional solid-state sintering where heat is absorbed to drive surface energy reduction, grain boundary migration, and pore elimination [29]. In

sharp contrast, the HM powder displays a strong and continuous exothermic event from ~800 K to 1500 K, with its heat flow rising from +0.2 W/g at 800 K to +3.5 W/g at 1500 K, where the increase becomes particularly sharp above 1200 K. Such a pronounced, sustained exotherm is a hallmark of the release of a large amount of stored internal energy accumulated during high-energy ball milling [30,31]. Specifically, the overall exothermic envelope can be schematically deconstructed: the modest heat release from 800 K to 1200 K likely corresponds to early-stage recovery processes such as dislocation motion and point defect recombination, while the sharp rise above 1200 K probably reflects more extensive structural reorganization. Significantly, such an intense and persistent exotherm in the high-temperature region suggests that the HM powder may undergo phase separation during subsequent sintering, as the excessive stored energy drives the system along a non-equilibrium transformation pathway [32]. Moreover, to achieve the same equilibrium phase assemblage as the conventionally PM-milled powder, a higher sintering temperature is likely required - one that supplies sufficient thermal energy to overcome the kinetic barrier imposed by the defect-rich, metastable state and to re-establish the thermodynamically stable single spinel phase. Collectively, the DSC results directly evidence that high-energy ball milling stores substantial internal energy in the pre-reacted spinel powder, which alters its thermal behavior and may necessitate an adjusted sintering protocol - particularly a higher final temperature - to obtain a phase-pure ceramic comparable to that processed by conventional milling.

3.3 Phase Evolution Regulated by Defects and Sintering Temperature

Fig. 4 presents the XRD patterns of the pre-sintered powder and the final sintered ceramic pellets. Solid-state reaction during pre-sintering at 850 °C yielded a powder with a well-developed spinel structure. This pre-sintered powder was subsequently ball-milled, crushed, and pressed into green bodies, which were then densified at 1250 °C. For ceramics prepared via conventional PM method, the XRD patterns of the final sintered pellets are identical to those of the pre-sintered spinel powder, demonstrating that the phase structure was retained throughout subsequent processing. In contrast, samples subjected to high-energy ball milling exhibited a distinct phase evolution behavior. XRD analysis reveals that when densified at 1250 °C, the HM-derived samples exhibit clear phase separation relative to the pre-sintered spinel structure. Upon further heating to 1280 °C, the enhanced atomic mobility allows the system to surmount this barrier via solid-state reaction among the secondary phases, re-establishing the equilibrium spinel. Indeed, increasing the sintering temperature from 1250 °C to 1280 °C enabled the high-energy ball milling-processed samples to yield XRD profiles and phase compositions consistent with both the planetary-ball-milled specimens (sintered at 1250 °C) and the pre-sintered powder. Research on Mn-Co-Ni-O spinel thermistor ceramics has shown that, for a fixed composition, grain size indeed influences the electrical resistivity of the material, and the direct driving force for grain refinement can originate from either compositional regulation or process optimization[33,34]. The results of the present study demonstrate that the high-energy ball milling (HM) process yields nano-sized powders with inherent resistance to grain

coarsening. Moreover, through optimization of the processing window (i.e., increasing the sintering temperature to 1280 °C), it is possible to achieve phase purity while retaining a sufficient contribution from grain boundaries [35].

3.4 Densification and Microstructure Controlled by Phase Purity

Fig. 5 a-d presents scanning electron microscopy (SEM) images of the surface and corresponding thermally etched (1200℃ for 10 min) cross-section of the thermosensitive ceramic tablets sintered at 1250℃. While the cross-section of the HM sample revealed no evident grain boundaries following identical thermal etching, the PM sample exhibited well-defined grain boundaries along with a uniform grain structure, having an average grain size in the micrometer range as determined by image analysis. The surface morphology after pelletizing and sintering corresponds to the morphology of the powder after secondary ball milling and crushing. For the sample processed by HM, the particle surface after pelletizing and sintering retains the irregular fractured surface from the crushing step. Moreover, compared with the ceramic surface formed by pelletizing and sintering the powder processed by PM, the sample from HM shows significantly fewer crack defects. The HM sample demonstrated a markedly denser structure compared to the PM sample. This distinction was evident from the minimal porosity observed in the HM sample against the numerous pores and microcracks at the particle/grain boundaries of the PM sample, as seen on both its as-sintered surface and thermally etched cross-section. The density measurement results further confirmed this structural advantage, with the HM sample achieving about 5.098

g/cm³, higher than the 4.341 g/cm³ of the PM sample.

As shown in Fig.6a, the resistivity of the thermistor ceramics prepared by two distinct ball-milling processes decreases with increasing temperature, exhibiting a negative temperature coefficient (NTC) characteristic. The differences in the ρ-T curves between the two processes originate from variations in the particle size distribution and particle microstructure of the precursor powders. Meanwhile, the linear fitting of lnρ versus 1000/T presented in Fig. 6b yields coefficients of determination (R^2) exceeding 0.9987 for both sample groups, strictly conforming to the Arrhenius equation. The electrical performance comparison between the two samples shows nearly identical activation energies (Ea ≈ 0.284 eV) and B constants (~3300 K), confirming that the small-polaron hopping mechanism is not affected by the ball-milling process. However, the HM sample exhibits a slightly lower room-temperature resistivity (ρ_{25} = 923.6 Ω·cm) than the PM sample (928.5 Ω·cm). This difference is attributed to the structural features induced by the HM process, including finer nanocrystalline grains, intragranular dislocations, and roughened particle surfaces. During sintering, these features promote densification and improve grain connectivity, thereby reducing the effective intergranular barrier and lowering the overall resistivity without altering the intrinsic activation energy.

3.6 Impedance Response and Carrier Transport Mechanism

To elucidate the influence of high-energy ball milling HM samples and PM samples on the electrical properties of NTC ceramics, impedance spectroscopy was performed at 273K, 253K and 233K (10 Hz~10 MHz). The data were geometrically normalized and, all Nyquist plots in Fig.7 show a single depressed semicircle that expands significantly with decreasing temperature, evidencing a typical negative temperature coefficient behavior. The equivalent circuit R_g (grain resistance) + R_{gb} (grain boundary resistance) // CPE was used for fitting, where the CPE (constant phase element) impedance is given by $Z_{CPE}= 1/[T(j\omega)^P]$, with T the pseudo-capacitance and P the dispersion exponent ($0<P\leq1$). Because the high-frequency intercept R_g exhibited non-monotonic temperature dependence due to contact resistance, the fitting was carried out using the fixed parameter values reported by Abram et al. [36]. The fitting results obtained from the equivalent circuit are given in Table 3. All fits were of high quality, yielding $\chi^2 < 5\times10^{-6}$ and relative errors for R_{gb} and P below 0.5%.

The grain boundary resistance R_{gb} for both HM and PM samples increases with decreasing temperature, and the HM samples consistently exhibit slightly lower R_{gb} than the PM samples. Arrhenius fitting gives activation energies of 0.272 ± 0.005 eV for HM samples and 0.278 ± 0.006 eV for PM samples; the difference lies within the combined errors, indicating that the barrier height Φ_B is statistically indistinguishable. According to the double-Schottky model, the barrier height Φ_B is proportional to the ratio of N_t/N_d; thus the two types of samples yield essentially the same N_t/N_d ratio. XRD shows that HM samples develop an intragranular metastable phase separation after sintering at 1250 °C, but this occurs inside the grains and does not alter the grain

boundary chemistry. The residual micropores in PM samples do not provide chemical interface states, hence they also do not affect Φ_B. As physical defects, pores can influence the migration paths and local electric field distribution of small polaron hopping, potentially modifying the pre-exponential factor, which is consistent with the observation of identical activation energies but slightly different R_{gb}. Although the two processes differ markedly in powder refinement and density, the grain boundary barrier heights converge, indicating that the barrier is primarily determined by the matrix composition and sintering temperature, and is not sensitive to the powder refinement method. The phase separation in HM samples causes no anomaly in R_{gb} or P, and raising the sintering temperature restores the equilibrium phase, confirming that the phase separation is merely a kinetic concomitant phenomenon that does not significantly affect grain boundary conduction. Therefore, HM samples slightly reduce the intrinsic R_{gb} by increasing density, but do not alter the barrier height, and thus have no substantial effect on the B value, in agreement with the measured resistance-temperature curves.

The dispersion exponent P shows a small but statistically discernible difference between the two types of samples (at 233K: HM samples 0.8151, PM samples 0.8124). A higher P indicates a narrower relaxation time distribution and a more concentrated frequency response. SEM reveals that HM samples are dense with very few pores, while PM samples contain isolated micropores. This is because the fragmented HM sample particles possess high surface energy and a high dislocation density (evidenced by discontinuous SAED rings), leading to rapid densification and a continuous, uniform

grain boundary network; the regular PM sample particles tend to bridge during packing, making pore elimination difficult. Pores can broaden the relaxation time distribution by interrupting grain boundary continuity, concentrating electric fields, and adsorbing charges, thereby lowering P. Consequently, the higher density of HM samples is the direct reason for their slightly higher P, implying that HM samples are more suitable for high-precision temperature measurement and fast temperature tracking applications.

4. Conclusion

In this work, $Mn_{1.25}Ni_{0.75}CoO_4$ thermosensitive ceramic was prepared using the solid-sate reaction route by using nano-oxide raw materials. The particle size evolution of nano-sized raw oxides during processing of Ni-Mn-Co-O based NTC thermistors was systematically followed, and the effects of two ball-milling processes on the microstructure and electrical properties were compared. The main findings are summarized as follows.

(1) The initial nano-sized oxides coarsen dramatically during the solid-state reaction. After pre-calcination, the particle size grows from about 50 nm to 955.4 nm, nearly a factor of 20. Thus the nanoscale advantage is essentially lost during solid-state reaction.

(2) High-energy ball milling applied after the solid-state reaction can refine the powder back to the nanoscale range (D_{50}: 58~78 nm). This process also creates a high density of intragranular dislocations, irregular particle surfaces, and increased internal energy, putting the powder into a non-equilibrium, metastable state. That state is manifested by

a strong, continuous exothermic event from about 800 K to 1500 K during thermal analysis.

(3) XRD reveals a metastable phase at 1250 °C in the HM samples, which transforms back to the equilibrium spinel phase at 1280 °C. Based on the analysis of Nyquist plots by equivalent circuit fitting, impedance analysis further shows that the grain boundary barrier height does not depend on the milling method, supporting the conclusion that this phase separation is only a kinetic concomitant phenomenon and does not affect grain boundary conduction.

(4) The fitted resistance-temperature characteristics are similar for both milling routes, and so are the B values. HM samples exhibit a slightly lower grain boundary resistivity due to their higher density, but the barrier height remains unchanged; consequently, the B value is not substantially affected. In other words, the barrier is not determined by the powder refinement method.

(5) HM samples are almost pore-free, whereas PM samples contain isolated micropores. On the other hand, high-energy ball milling tends to cause localized abnormal grain growth and a rougher surface on the sintered bodies, indicating that further optimization of process parameters is necessary to suppress microstructural inhomogeneity.

Overall, this study demonstrates that by appropriate coordination of ball milling and sintering, the final microstructure and properties of thermosensitive ceramics can be effectively tailored. This provides a solid technological basis for the preparation of high-performance NTC thermistors. Future work should further investigate the effects

of milling parameters on grain boundary architecture and explore the long-term stability of HM-processed thermistors under thermal cycling.

Acknowledgements

This work was supported by Central Government Guidance Fund for Local Sci-Tech Development (ZYYD2025ZY08), Natural Science Foundation of Xinjiang Uygur Autonomous Region (Grant No.2025D01A135) and the Tianshan Talent - Science and Technology Innovation Leading Talent Project (2024TSYCLJ0037).

References

[1] K. Park, S.J. Kim, J.G. Kim, et al., Structural and electrical properties of MgO-doped $Mn_{1.4}Ni_{1.2}Co_{0.4-x}Mg_xO_4$ ($0 \leq x \leq 0.25$) NTC thermistors, J. Eur. Ceram. Soc. 27 (2007) 2009-2016. DOI:10.1016/j.jeurceramsoc.2006.07.002.

[2] Y. Yang, Y. Pu, M. Chen, R. Peng, H. Wu, D. Wu, Exploring the influence of phase transition and grain size on the structural and electrical properties of $NaNbO_3$ ceramics, Ceram. Int. 51 (2025) 37009-37018. DOI:10.1016/j.ceramint.2025.05.411.

[3] A. Feteira, Negative temperature coefficient resistance (NTCR) ceramic thermistors: an industrial perspective, J. Am. Ceram. Soc. 92 (2009) 967-983. DOI:10.1111/j.1551-2916.2009.02990.x.

[4] Z. Song, Z. Chen, G. Du, et al., Research progress on negative temperature coefficient thermistors: review, J. Mater. Sci. Mater. Electron. 36 (2025) 1. DOI:10.1007/s10854-025-14727-w.

[5] B.Y. Price, Tekeli, G. Hardal, Electrical properties of $Ni_{0.5}Co_{0.8}Mn_{1.7}O_4$ and $Ni_{0.5}Co_{1.1}Mn_{1.4}O_4$ negative temperature coefficient ceramics doped with B_2O_3, J. Mater. Sci.: Mater. Electron. 32 (2021) 8983–8990. DOI:10.1007/s10854-021-05569-3

[6] F. Zhang, Z.M. Huang, Effects of partial substitution of cations on electrical properties of Mn-Co-Ni-O thin films, Appl. Phys. Lett. 111 (2017) 222103. DOI:10.1063/1.5004035.

[7] H.-S. Han, H. Lee, J. Lim, et al., Hopping conduction in $(Ni,Co,Mn)O_4$ prepared by different synthetic routes: conventional and spark plasma sintering, Ceram. Int. 43 (2017) 16070-

16075. https://doi.org/10.1016/j.ceramint.2017.08.105.

[8] R. Schmidt, A. Basu, and A. W. Brinkman, Small polaron hopping in spinel manganates, Phys. Rev. B. 72, 115101 (2005). DOI:10.1103/PhysRevB.72.115101.

[9] J. Wang, J. Yao, Z Chen, et al., Effects of Sr-doping on the electrical properties of $MnCoNiO_4$ NTC ceramics. J. Mater. Sci.: Mater. Electron. 24, 622-627 (2013). DOI:10.1007/s10854-012-0776-8.

[10] J. Xia, Q. Zhao, B. Gao, et al., Preparation and electrical properties of $Mn1.05\text{-}yCo_{1.95\text{-}x\text{-}z\text{-}w}Ni_xMg_yAl_zFe_wO_4$ NTC ceramic derived from microemulsion method, J. Alloys Compd. 591 (2014) 207–212. https://doi.org/10.1016/j.jallcom.2013.12.021

[11] Y. Wei, B. Zhang, Z. Fu, et al., Synthesis and high thermal stability of Mn doped $Y_{2/3}Cu_3Ti_4O_{12}$ negative temperature coefficient ceramic, J. Solid State Chem. 303 (2021) 122536. DOI:10.1016/j.jssc.2021.122536.

[12] S. Liang, C. Cao, H. Liang, X. Yi, J. Xiao, One-step synthesis of Ni-Mn-Al-O thin film on Al2O3 substrate via hydrothermal method, Microelectron. Eng. 182 (2017) 53-56. DOI:10.1016/j.mee.2017.09.002.

[13] B. Y. Price, S.R. Kennedy, Resonant acoustic-mixing technology as a novel method for production of negative-temperature coefficient thermistors, J. Mater. Sci.: Mater. Electron. 33 (2022) 11380-11391. DOI:10.1007/s10854-022-08110-2

[14] S. Liang, J.F. Yang, X.H. Yi, J. Xiao, An efficient way to improve the electrical stability of $Ni_{0.6}Si_{0.2}Al_{0.6}Mn_{1.6}O_4$ NTC thermistor, Ceram. Int. 37 (2011) 2537-2541. https://doi.org/10.1016/j.ceramint.2011.03.061.

[15] Z. Fu, Y. Wei, Y. Liu, B. Zhang, S. Huang, A. Chang, Polycrystalline thermosensitive ceramic oxides in $CaCeNbWO_8$: density, texture, and thermal aging stability, J. Am. Ceram. Soc. 105 (2022) 2442-2453. https://doi.org/10.1111/jace.18244.

[16] T. Yang, B. Zhang, Q. Zhao, et al., Vacuum hot pressed highly dense, nanograined $Mg(Al_{1-x}Cr_x)_2O_4$ ceramics, Mater. Lett. 194 (2017) 42-44. DOI:10.1016/j.matlet.2017.02.010.

[17] B. Wang, A. Chang, J. Wang, Y. Wang, H. Wu, Influence of particle size on the structural and electrical properties of $Mn_{1.1}Co_{1.5}Fe_{0.4}O_4$ ceramics, Scr. Mater. 188 (2020) 254-258. https://doi.org/10.1016/j.scriptamat.2020.07.012.

[18] S.M. Hosseini, B.G. Shohany, N. Azad, et al., Electrical properties comparison of NTC thermistors prepared from nanopowders and in mixed oxide process, Mater. Sci.-Pol. 29 (2011) 253-259. DOI:10.2478/S13536-011-0039-Z.

[19] B. Wang, J. Wang, A. Chang, Y. Wang, H. Wu, Effects of particle sizes of starting oxides on the properties of spinel-type $Mn_{1.1}Co_{1.5}Fe_{0.4}O_4$ negative temperature coefficient ceramics, Ceram. Int. 47 (2021) 2531-2537. https://doi.org/10.1016/j.ceramint.2020.09.097.

[20] T. Yokoyama, T. Meguro, Fabrication and electrical properties of sintered bodies composed of $Mn_{1.75-1.25x}Co_{2.5x}Ni_{1.25(1-x)}O_4$ ($0 \leq x \leq 0.6$) with a cubic spinel structure, J. Ceram. Process. Res. 10 (2009) 683-688. DOI : 10.36410/jcpr.2009.10.5.683.

[21] T. Yokoyama, T. Meguro, Y. Shimada, Preparation and electrical properties of sintered oxides composed of $Mn_{1.5}Co_{0.25+x}Ni_{1.25-x}O_4$ ($0 \leq x \leq 0.75$) with a cubic spinel structure, J. Mater. Sci. 42 (2007) 5860-5866. https://doi.org/10.1007/s10853-006-1141-1.

[22] C. Peng, H. Zhang, A. Chang, et al., Microstructure and electrical properties of $Mn_{2.25-x}Ni_{0.75}Co_xO_4$ thermosensitive ceramics, J. Inorg. Mater. 26 (2011) 1037-1042. DOI:10.3724/SP.J.1077.2011.01037.

[23] A. Feltz, J. Töpfer, F. Schirrmeister, Conductivity data and preparation routes for NiMn2O4 thermistor ceramics, J. Eur. Ceram. Soc. 9 (1992) 187-191. DOI:10.1016/0955-2219(92)90004-w.

[24] K. Fujiwara, S. Lee, N. Donnelly, C.A. Randall, Resistance degradation in $Y(Cr,Mn)O_3$-Y_2O_3 composite NTC ceramics in hostile environments, J. Am. Ceram. Soc. 92 (2009) 2634-2641. DOI: 10.1111/j.1551-2916.2009.03264.x.

[25] S.A. Fatima, M.N. Khan, R. Shaheen, et al., Temperature dependent AC-conduction and relaxation mechanism of spinel $MgCo_2O_4$ system by impedance spectroscopy, Phys. B 600 (2021) 412581. DOI: 10.1016/j.physb.2020.412581.

[26] C.-L. Yuan, X.-Y. Liu, J.-Y. Huang, X. Liu, Electrical properties and impedance analysis of $Bi_{0.5}Ba_{0.5}FeO_3$ ceramic, Acta Phys. Sin. 60 (2011) 025201. DOI: 10.7498/aps.60.025201.

[27] N. Hashimoto, K. Mori, H. Yoshida, et al., Thermal stability of high-entropy alloy nanoparticles evaluated by in situ TEM observations, Nano Lett. 24 (2024) 6. DOI:10.1021/acs.nanolett.4c01625.

[28] D.L. Zhang, Processing of advanced materials using high-energy mechanical milling, Prog. Mater. Sci. 49 (2004) 537-560. DOI:10.1016/S0079-6425(03)00034-3.

[29] J. Xia, W. Ren, H. Sun, A. Chang, B. Zhang, Fabrication of Mn-Co-Ni-O NTC ceramics via reactive flash sintering at ultralow temperature, Ceram. Int. 50 (2024) 16111-16117. https://doi.org/10.1016/j.ceramint.2024.02.091.

[30] C.C. Koch, Synthesis of nanostructured materials by mechanical milling: problems and opportunities, Nanostruct. Mater. 9 (1997) 13-22. DOI:10.1016/S0965-9773(97)00014-7.

[31] A.A. Al-Tabbakh, N. Karatepe, A.B. Al-Zubaidi, et al., Crystallite size and lattice strain of lithiated spinel material for rechargeable battery by X-ray diffraction peak-broadening analysis, Int. J. Energy Res. 43 (2019) 1903–1911. DOI:10.1002/er.4390.

[32] N. Obradović, W.G. Fahrenholtz, S. Filipović, et al., The effect of mechanical activation on synthesis and properties of $MgAl_2O_4$ ceramics, Ceram. Int. 45 (2019) 12015-12021. https://doi.org/10.1016/j.ceramint.2019.03.095.

[33] L. He, Z.Y. Ling, Electrical conduction of intrinsic grain and grain boundary in Mn-Co-Ni-O thin film thermistors: grain size influence, J. Appl. Phys. 110 (2011) 093708. https://doi.org/10.1063/1.3657772.

[34] M.M. Cui, X. Zhang, K.G. Liu, et al., Fabrication of nano-grained negative temperature coefficient thermistors with high electrical stability, Rare Met. 40 (2021) 1014-1019. DOI:10.1007/s12598-019-01294-3.

[35] A.I. Gusev, High-energy ball milling of nonstoichiometric compounds, Phys.-Usp. 63 (2020) 342-364. DOI:10.3367/UFNe.2019.06.038581.

[36] E.J. Abram, D.C. Sinclair, A.R. West, A strategy for analysis and modelling of impedance spectroscopy data of electroceramics: doped lanthanum gallate, J. Electroceram. 10 (2003) 165-177. DOI:10.1023/B:JECR.0000011215.56084.87.

Tables and figure captions

Table1 Particle size data monitored after pre-sintering and before final pressing/sintering during powder processing via two different mixing and ball milling routes. (The fitted R^2 values for the particle size measurements range from 0.98 to 0.99.)

Table2 Parameters obtained from linear regression of lnρ on 1000/T

Table3 Equivalent circuit fitting parameters for HM and PM samples at different temperatures, with R_g fixed to the high-frequency intercept.

Figure 1. Preparation process of thermistor ceramics based on solid-state reaction.

Figure 2. Powder particle morphology and size distribution in the preparation of thermosensitive ceramics (Fitting was performed on the particle size distribution test results). (a) Morphology of pre-sintered particles; Subsequently, the pre-sintered powder was separately subjected to (b) planetary ball milling and (d) high energy ball milling; c) and e) HRTEM images of the particles displayed in (b) and (d), with insets featuring their internal lattice structure and corresponding diffraction pattern.

Figure 3. DSC curves of the samples ball-milled by the HM and PM methods.

Figure 4. Phase composition of the pre-sintered powders and the thermally sensitive ceramics after secondary high-temperature sintering.

Figure 5. The surface and cross-sectional morphology images of the thermosensitive ceramic tablets fabricated by different routes. (The polished cross-section samples were thermally etched at 1000℃ for 7min.)

Figure 6. (a) Temperature-dependent resistivity characteristics of ceramics; (b) the relationship between the natural logarithm of resistivity (lnρ) and the inverse of absolute temperature (1000/T).

Figure 7. The complex impedance spectra of the $Mn_{1.25}Ni_{0.75}CoO_4$ thermosensitive ceramics, fabricated via two distinct ball milling processes, measured at 273K, 253K and 233K.

Table 4 Particle size data monitored after pre-sintering and before final

pressing/sintering during powder processing via two different mixing and ball milling routes. (The fitted R^2 values for the particle size measurements range from 0.98 to 0.99.)

Fabrication route	Particle size		
	Measurement results		Fitting results
	D_{50}(nm)	D_{90}(nm)	D(nm)
Pre-sintered	955.4	1106.4	971±3.1
PM	1106.4	1483.9	1205.2±5.3
HM	50.7	78.8	58.2±3.7

Table 5 Parameters obtained from linear regression of lnρ on 1000/T

Sample	Slope	Intercept	R^2	E_a(eV)	B(K)	ρ_0 (Ω·cm)	$B_{25/50}$ (K)	ρ_{25} (Ω·cm)
HM	3.30614	-4.48618	0.99872	0.2849	3306.14	0.01127	3678	923.644
PM	3.28941	-4.42402	0.99874	0.2835	3289	0.01199	3660	928.4668

Table 6 Equivalent circuit fitting parameters for HM and PM samples at different temperatures, with R_1 fixed to the high-frequency intercept.

Sample	Temperature (K)	R_1 (Ω)	R_2 (Ω)	CPE-T ($F \cdot s^{n-1}$)	CPE-P	C_{eff} (pF)

	273	6.30	554.9	9.43×10^{-11}	0.8756	9.6
HM	253	91.3	1272	1.63×10^{-10}	0.8423	9.1
	233	96.5	3908	1.81×10^{-10}	0.8213	8.4
	273	5.77	537.1	9.27×10^{-11}	0.8806	9.6
PM	253	125.1	1213	1.48×10^{-10}	0.8555	10.7
	233	55.6	3978	2.32×10^{-10}	0.8092	8.8



High-purity oxide feedstocks



Weighing



Planetary ball mill machine

Mixing

Drying



Pre-sintering





Planetary ball mill machine



High-energy ball mill machine

Particle size reduction

Drying



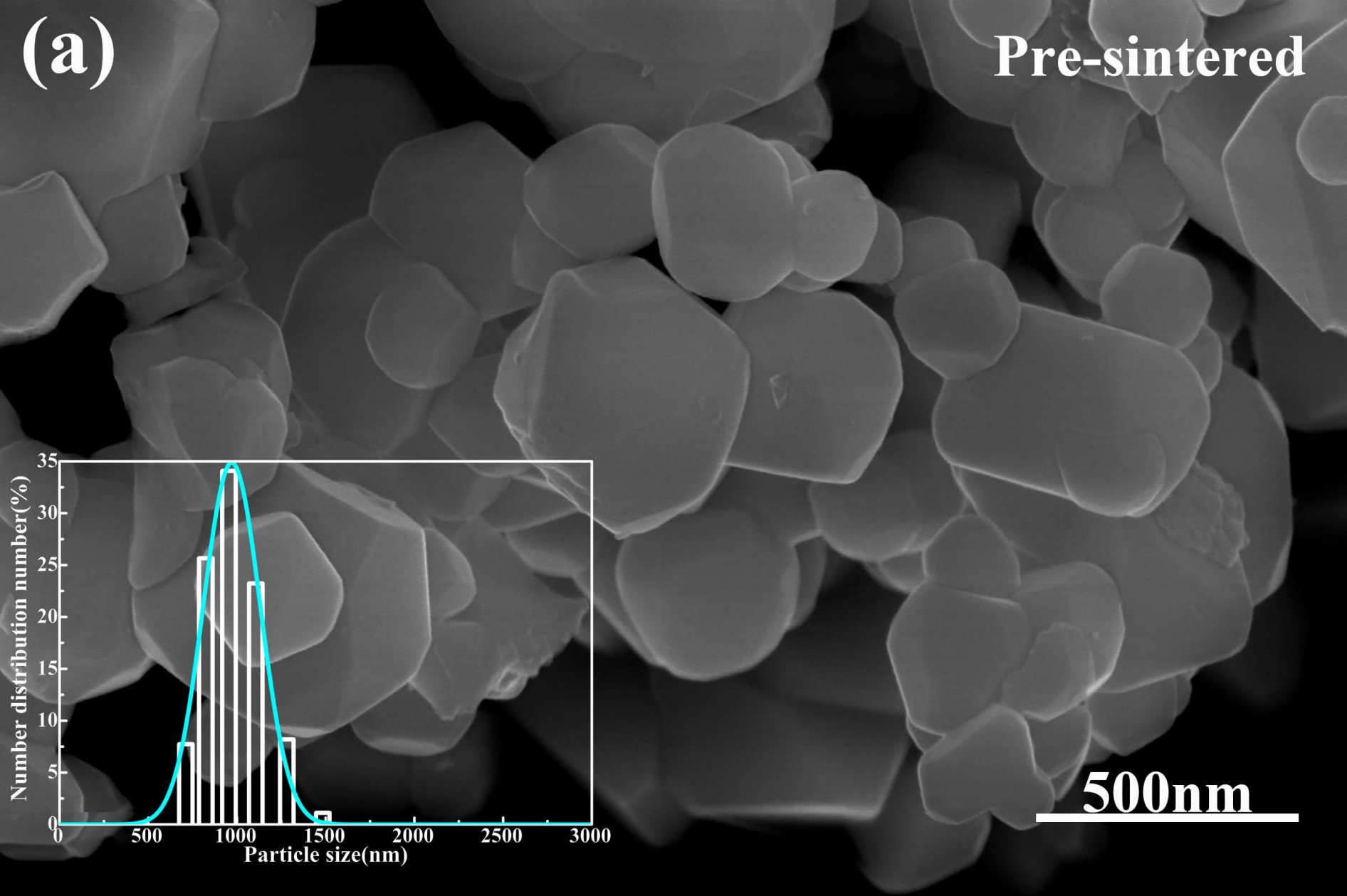
Pressing into pellets

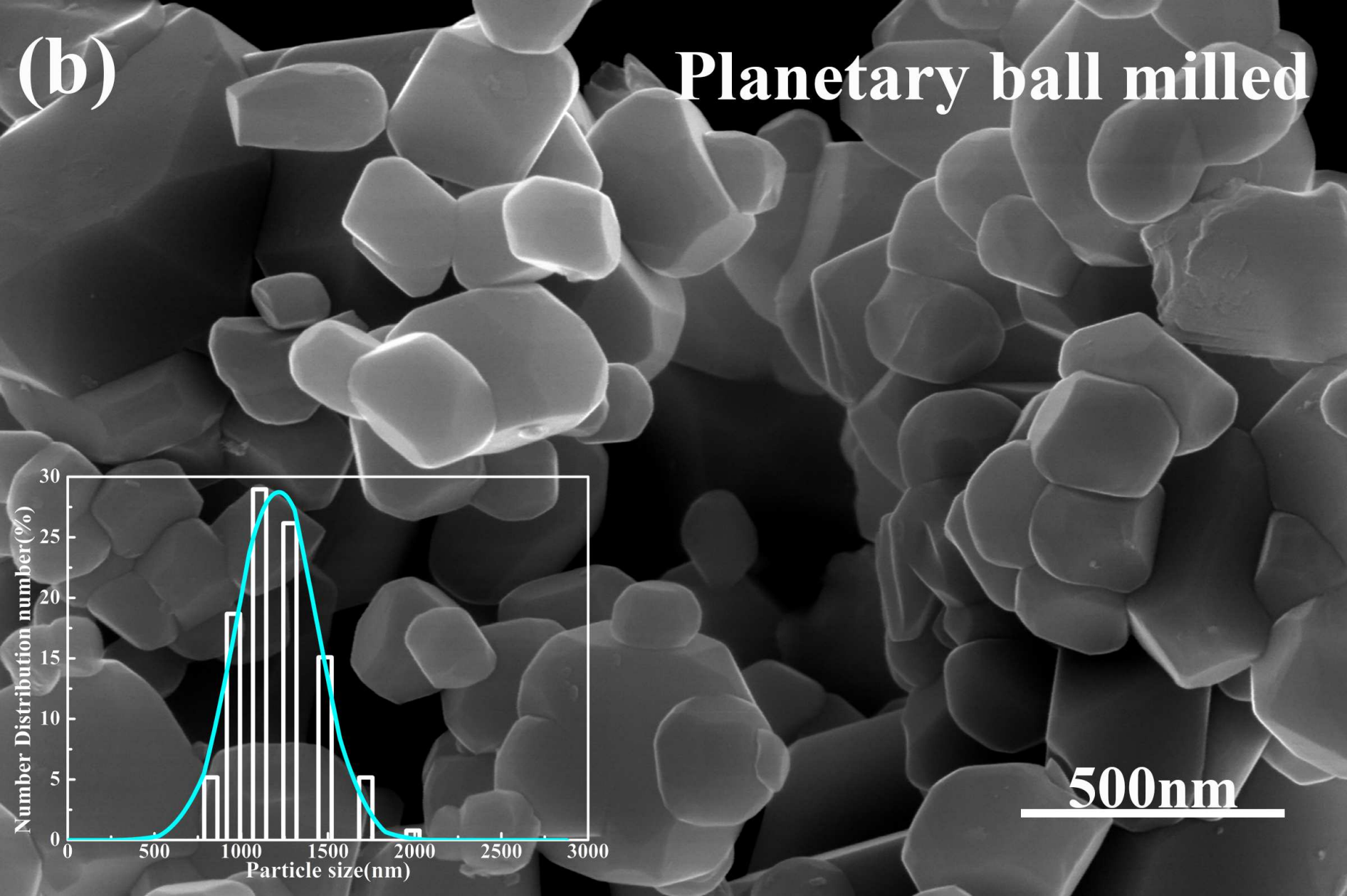


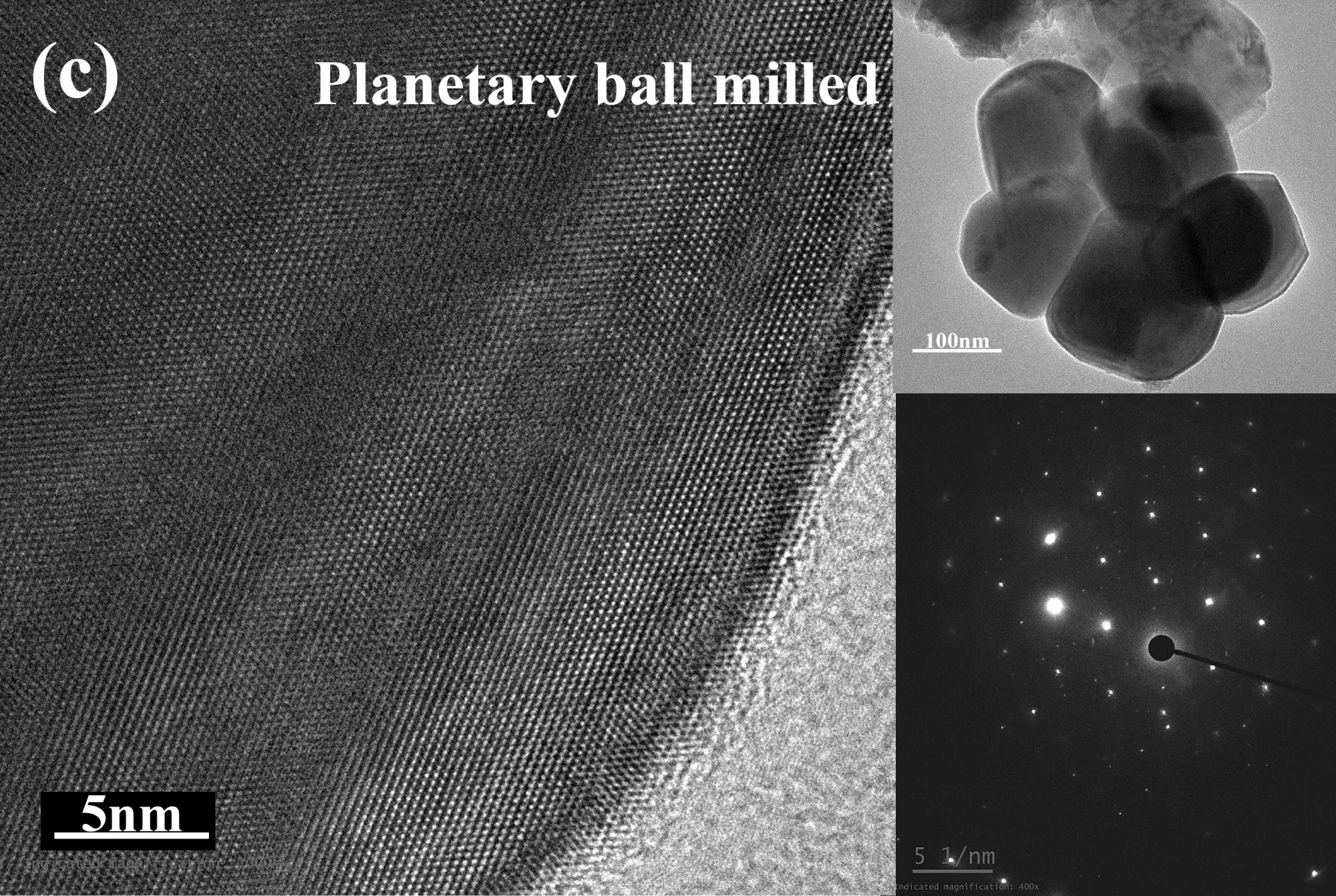
Sintering

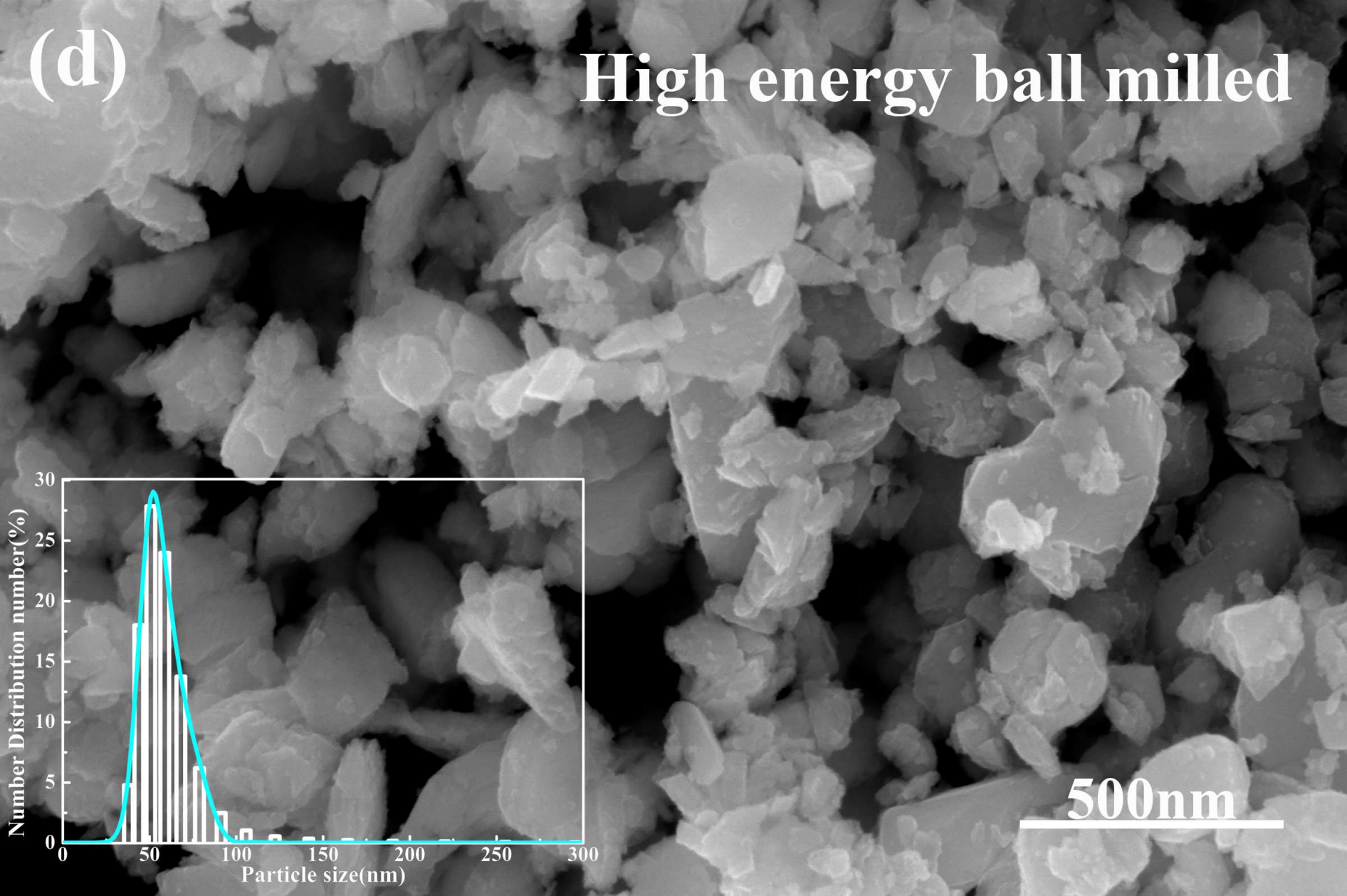


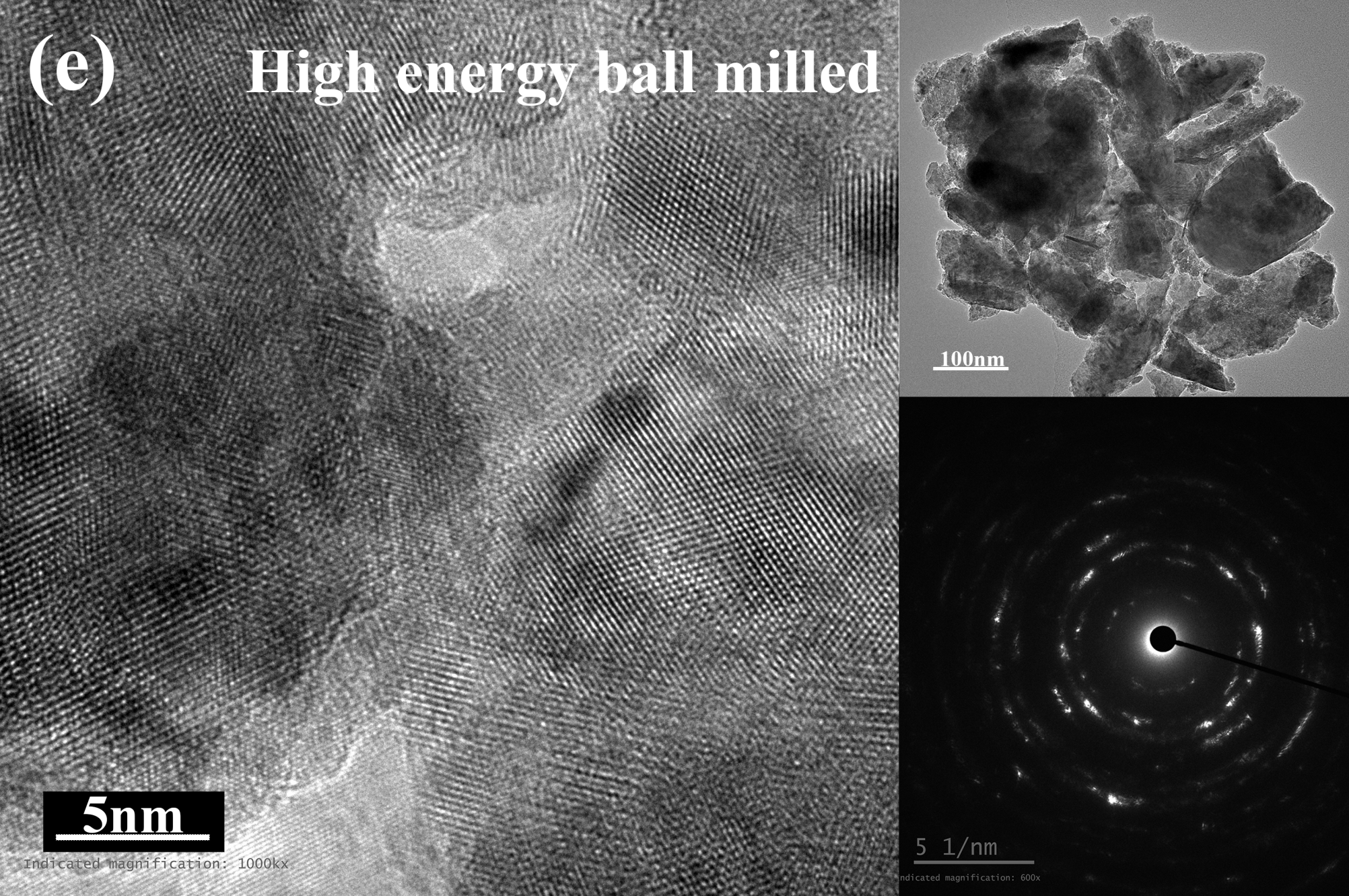


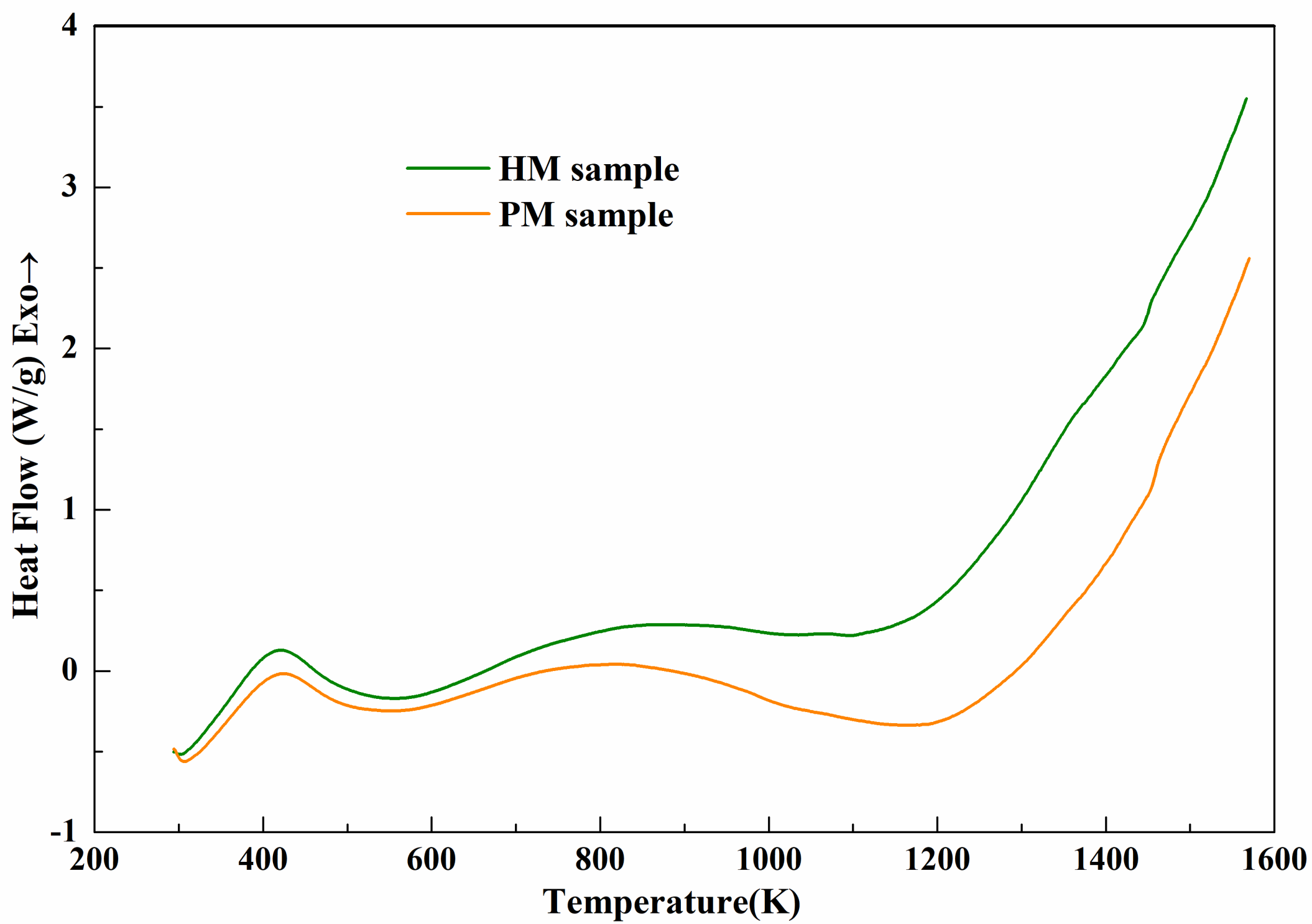

(a)
Pre-sintered
Number distribution number(%)
0
5
10
15
20
25
30
35
0
500
1000
1500
2000
2500
3000
Particle size(nm)
500nm

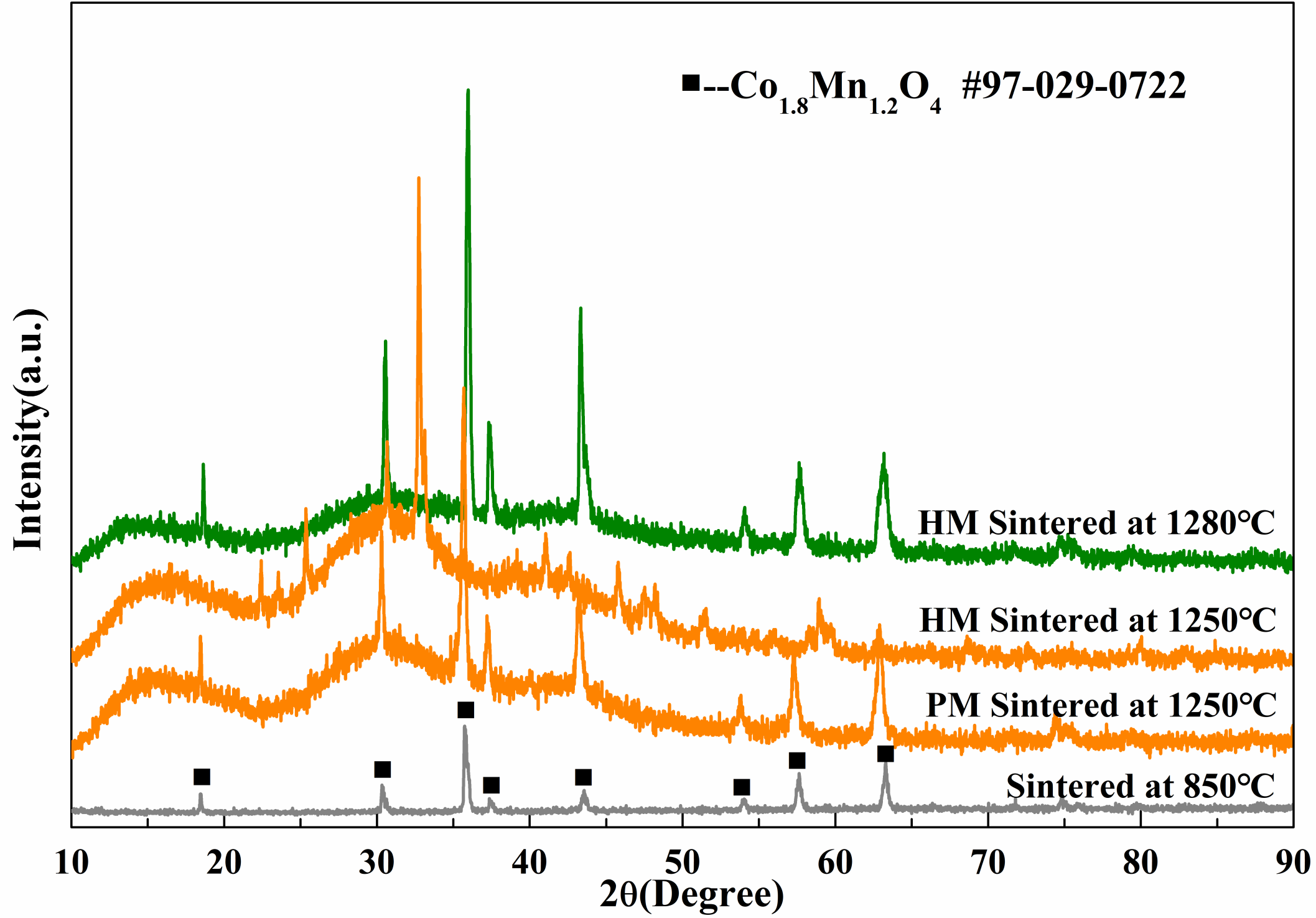

(b)
Planetary ball milled
Number Distribution number(%)
30
25
20
15
10
5
0
0
500
1000
1500
2000
2500
3000
Particle size(nm)
500nm

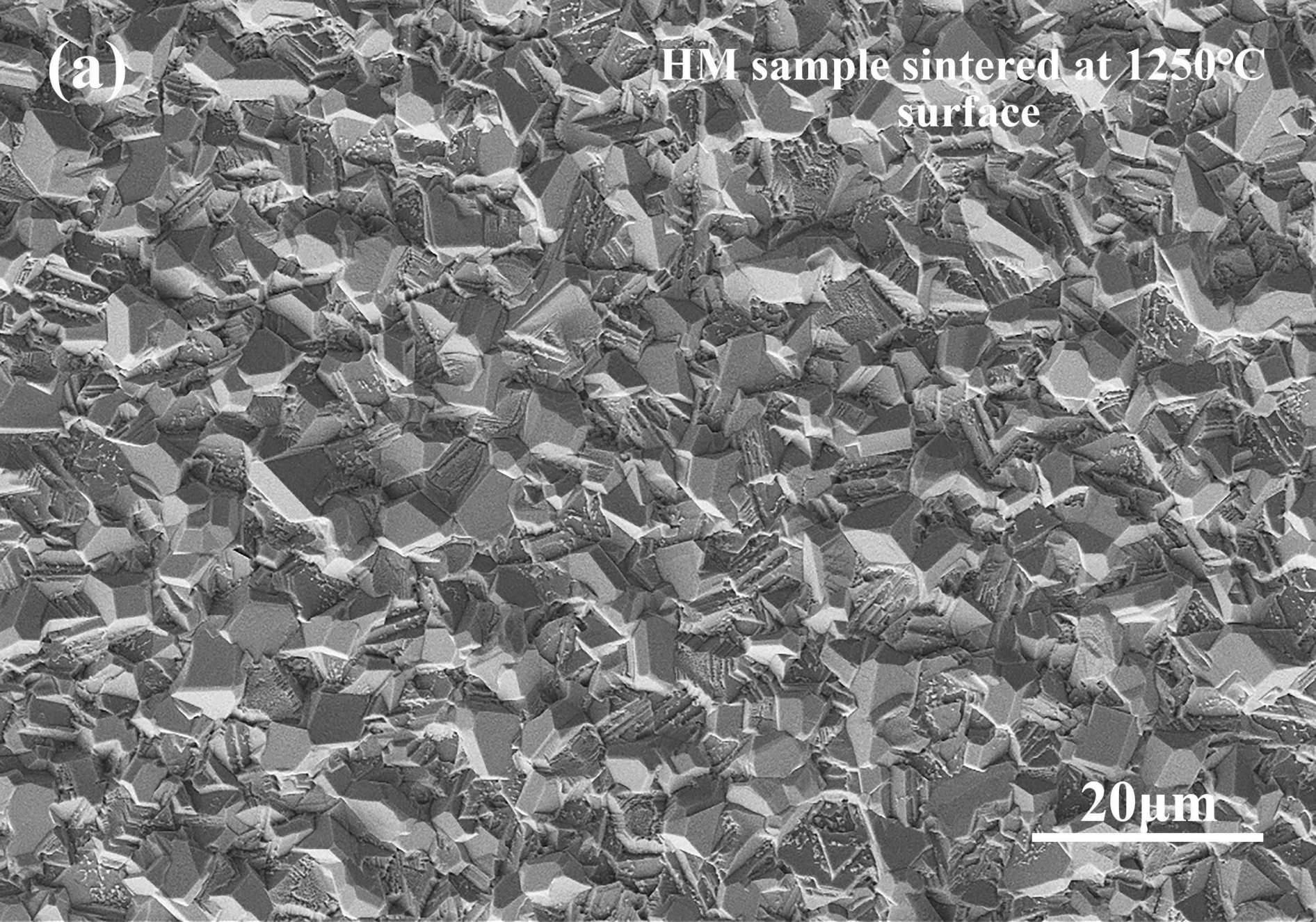

(c)
Planetary ball milled
5nm
100nm
5 1/nm

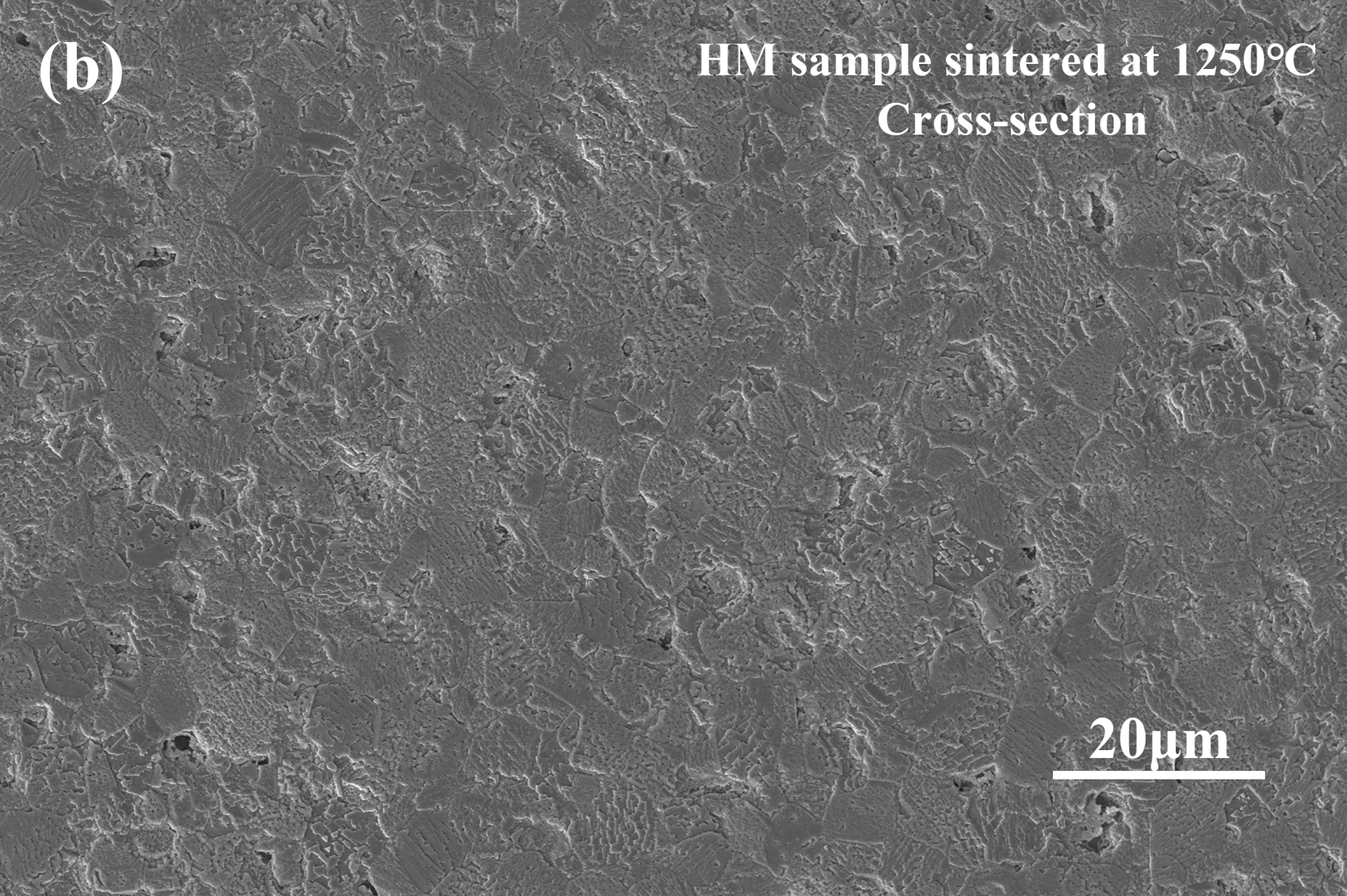

(d)
High energy ball milled
Number Distribution number(%)
0
5
10
15
20
25
30
0
50
100
150
200
250
300
Particle size(nm)
500nm

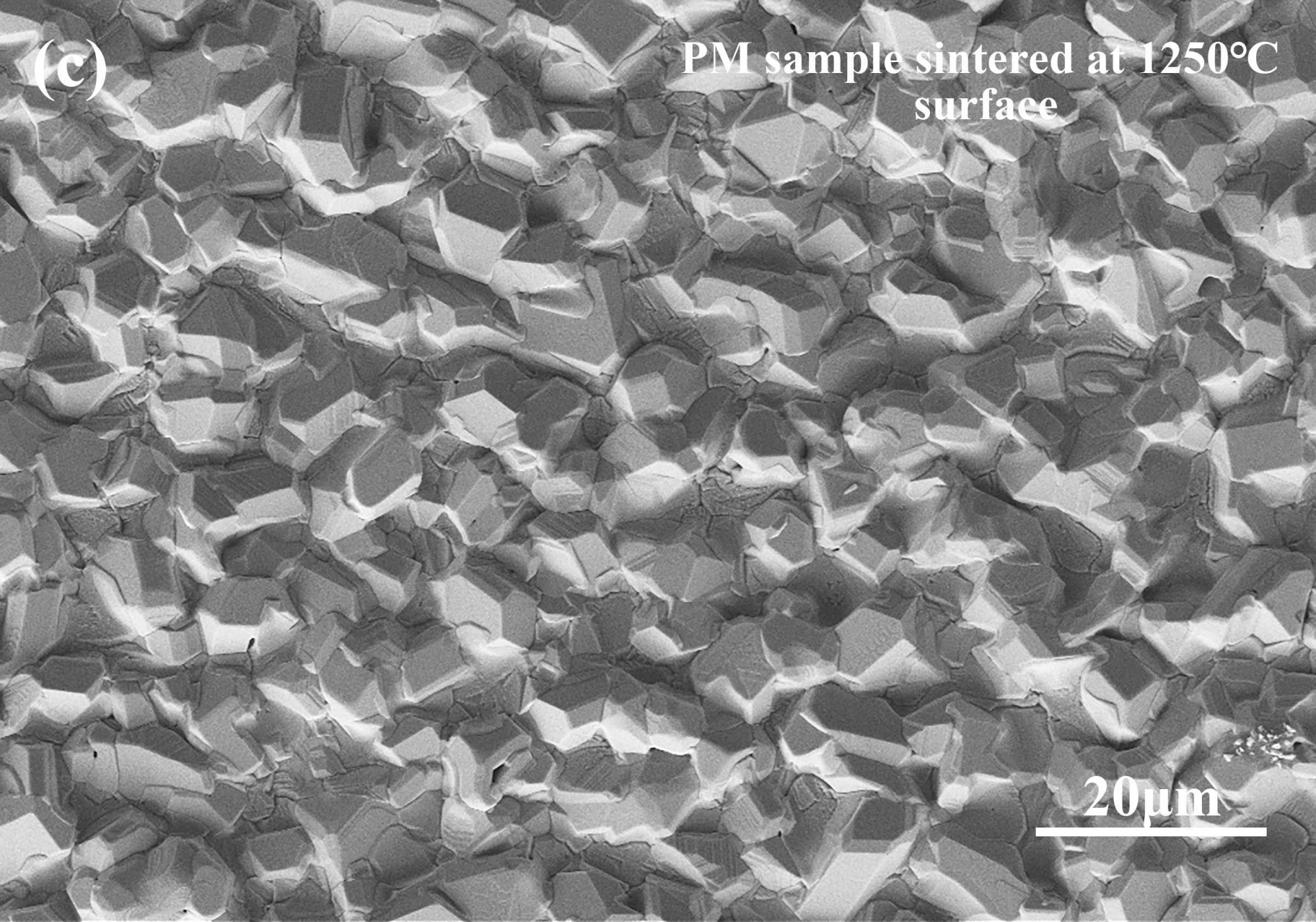

(e)
High energy ball milled
5nm
Indicated magnification: 1000kx
100nm
5 1/nm
Indicated magnification: 600x

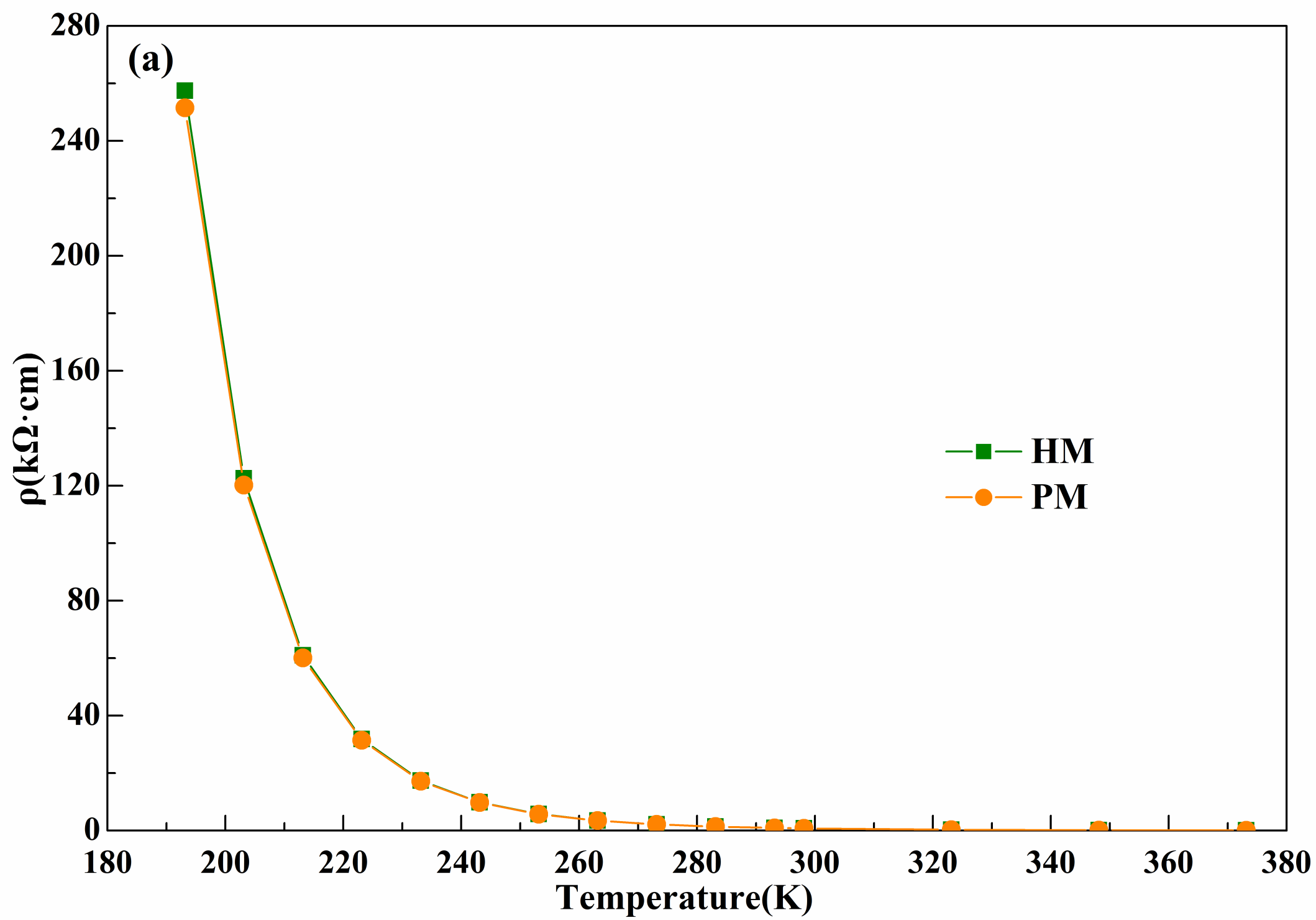

HM sample
PM sample
Heat Flow (W/g) Exo→
Temperature(K)
4
3
2
1
0
-1
200
400
600
800
1000
1200
1400
1600

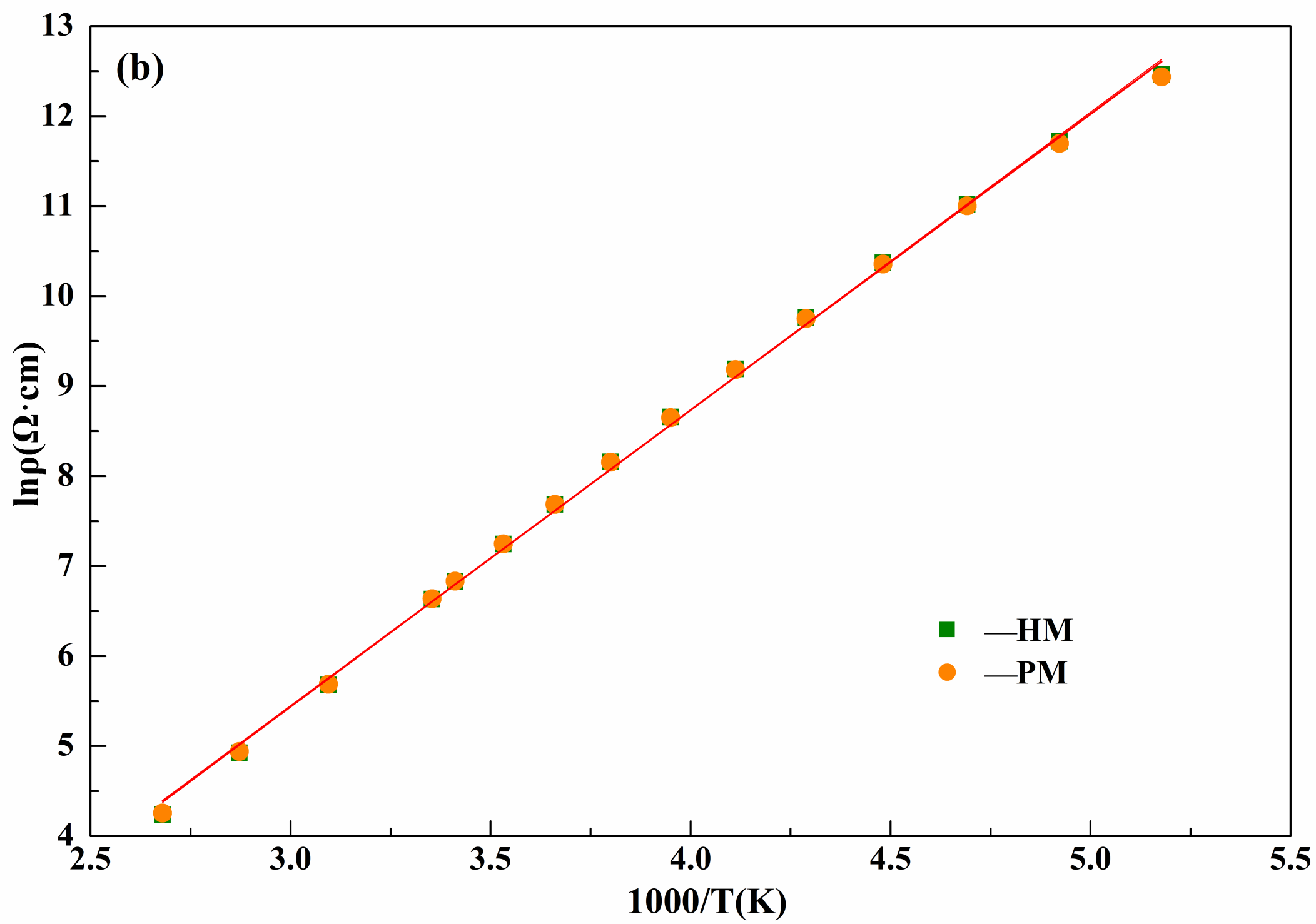

■--Co1.8Mn1.2O4 #97-029-0722
HM Sintered at 1280℃
HM Sintered at 1250℃
PM Sintered at 1250℃
Sintered at 850℃
Intensity(a.u.)
10
20
30
40
50
60
70
80
90
2θ(Degree)

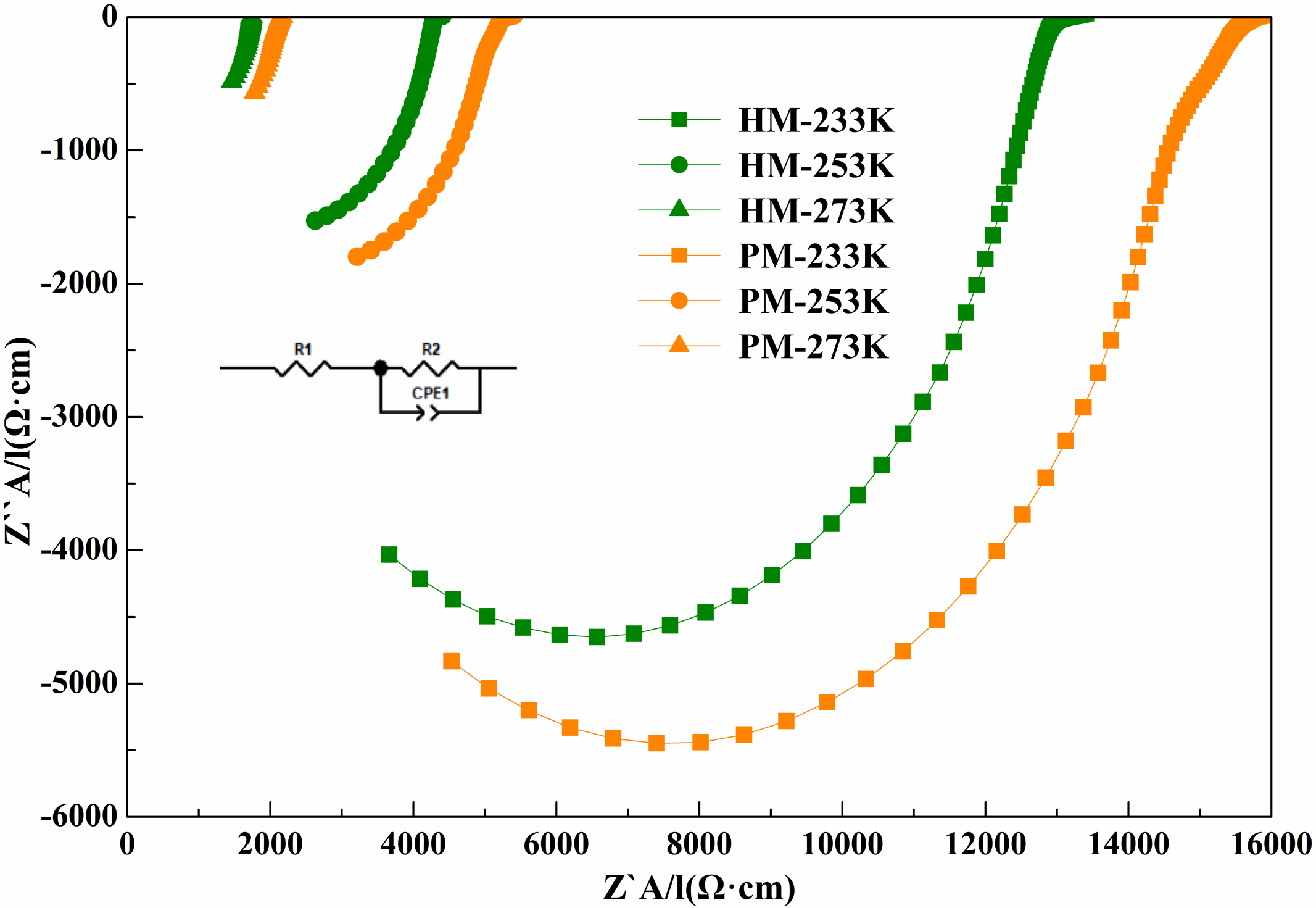

(a)
HM sample sintered at 1250°C
surface
20μm


(b)
HM sample sintered at 1250°C
Cross-section
20µm


(c)
PM sample sintered at 1250°C
surface
20μm


(a)
ρ(kΩ·cm)
280
240
200
160
120
80
40
0
180
200
220
240
260
280
300
320
340
360
380
Temperature(K)
HM
PM


(b)
lnρ(Ω·cm)
1000/T(K)
—HM
—PM
13
12
11
10
9
8
7
6
5
4
2.5
3.0
3.5
4.0
4.5
5.0
5.5


HM-233K
HM-253K
HM-273K
PM-233K
PM-253K
PM-273K
R1
R2
CPE1
Z``A/l(Ω·cm)
Z`A/l(Ω·cm)
0
-1000
-2000
-3000
-4000
-5000
-6000
0
2000
4000
6000
8000
10000
12000
14000
16000